Research Square

Preprints are preliminary reports that have not undergone peer review.
They should not be considered conclusive, used to inform clinical practice,
or referenced by the media as validated information.

Generalized photoactivatable fluorescent probes for background-suppressed single-molecule and live-cell imaging

Huang Tang
Nanjing University
Shuting Liu
Nanjing University
Xi Zhang
Nanjing University
Chenyue Kang
Nanjing University
Xing-Hua Xia
Nanjing University https://orcid.org/0000-0001-9831-4048
Boyang Hua
danfenzi.h@nju.edu.cn
Nanjing University https://orcid.org/0009-0001-6488-6096

Article

Keywords: photoactivatable fluorescent probes, PhADE, background suppression, concentration barrier, single-molecule imaging, hydrogels, single-particle tracking, live cells

Posted Date: November 17th, 2026

DOI: https://doi.org/10.21203/rs.3.rs-9070027/v3

License: This work is licensed under a Creative Commons Attribution 4.0 International License.
Read Full License

Additional Declarations: The authors declare no competing interests.

Generalized photoactivatable fluorescent probes for background-suppressed single-molecule and live-cell imaging

Huang Tang,[a,b,1] Shuting Liu,[a,b,1] Xi Zhang,[a,b] Chenyue Kang,[a,b] Xing-Hua Xia,[a,b,*] Boyang Hua[a,b,*]

[a]School of Chemistry, Nanjing University, Nanjing, 210023, China
[b]State Key Laboratory of Analytical Chemistry for Life Science, Nanjing University, Nanjing, 210023, China

[1]H.T., and S.L. contributed equally to this work.
[*]To whom correspondence may be addressed.
Emails: xhxia@nju.edu.cn (X.X.); danfenzi.h@nju.edu.cn (B.H.)

Abstract

Many single-molecule and super-resolution imaging techniques require efficient and precise spatiotemporal control of fluorescence, yet photoactivatable (PA) fluorophores remain limited in choice, owing to their commercial availability, complex custom synthesis routes, and in some cases suboptimal photophysical and photochemical properties. Here, we present a class of generalized and modular PA fluorescent probes based on DNA scaffolds. These probes are readily accessible, flexible with fluorophore cores and attachment moieties, and have improved performance over existing PA fluorophores. With these probes, we implement background-suppressed single-molecule imaging in hydrogels, overcoming the "concentration barrier", as well as real-time single-vesicle tracking in live cells. These versatile PA probes could facilitate wider adoption of many advanced imaging techniques.

Keywords

photoactivatable fluorescent probes; photoactivation, diffusion, and excitation; background suppression; concentration barrier; single-molecule imaging; hydrogels; single-particle tracking; live cells

Introduction

Photoactivatable (PA) probes are indispensable reagents for many single-molecule and super-resolution imaging techniques, where precise and efficient spatiotemporal control of fluorescence emission is key to achieve the full capabilities of these methods.[1-10] For instance, to overcome the long-standing "concentration barrier" in single-molecule fluorescence imaging,[11, 12] the photoactivation, diffusion, and excitation (PhADE) strategy[1] exploits PA probes to ensure that only bound molecules emit fluorescence, while most unbound molecules remain in the dark state to avoid contributing to the background fluorescence. Although initially demonstrated with TIRF microscopy for surface-proximal imaging, PhADE, in principle, can be extended to deep volumetric imaging when combined with confocal or light-sheet microscopy. In addition, PA probes have become central to modern super-resolution microscopy, such as (fluorescence) photoactivated localization microscopy [(f)PALM],[4, 5] single-particle tracking PALM (sptPALM),[6] patterned activation nonlinear structured illumination microscopy (PA NL-SIM),[7] and minimal photon FLUX (MINFLUX).[8] Commonly in these techniques, only a sparse subset of PA probes are activated at any given time, allowing individual molecules to be localized or tracked beyond the diffraction limit.

Consequently, the development of high-performance PA probes has been of keen interest in the field. PA probes are broadly categorized into fluorescent proteins and synthetic fluorophores. While fluorescent proteins can be genetically encoded,[13, 14] synthetic fluorophores are generally brighter and more photostable,[3, 15-22] making them particularly attractive for demanding imaging applications. Among synthetic PA probes, rhodamine-based fluorophores are among the most extensively explored, offering a color palette spanning the visible spectrum through structural tuning.[19-22] However, several rhodamine-based fluorophores, including the PA JF series, can exhibit photophysical artifacts, such as blinking,[23] and have limited photoactivation efficiencies, which may complicate quantitative image analysis and motivate the development of other classes of synthetic PA probes. A modular design strategy has been developed in which a fluorophore is covalently linked to a quencher through a photolabile linker, enabling fluorescence "off-on" control across various fluorophore cores.[3, 17-20] Although powerful and versatile, most synthetic PA probes require relatively complex organic synthesis routes, rendering them difficult to access unless commercially available and limiting their broader application in photoactivation-based biophysical methods.

In this study, we generated a class of modular, readily accessible, and versatile PA probes, named the fluorophore-quencher-DNA (FQD) probes. As a common advantage of DNA-scaffolded fluorescent probes (e.g., CFOs, FluoroCubes, and FRETfluors),[17, 24, 25] the fluorescence, quenching, and attachment moieties of FQD are structurally and functionally decoupled, so each component can be individually varied. Photoactivation experiments in bulk and at the single-molecule level demonstrate that FQD probes exhibit an excellent on-off intensity ratio and can be activated by mild UV illumination with an efficiency surpassing that of some existing PA fluorophores. Using FQD probes, we implemented PhADE in combination with confocal microscopy (confocal PhADE) and achieved deep volumetric single-molecule imaging of rolling circle amplification (RCA) and DNA hybridization in hydrogels, suppressing background fluorescence even in the presence of high concentrations of labeled probes. In live cells, we further demonstrate real-time single-particle tracking of endocytosed cation-independent mannose 6-phosphate receptor (CI-M6PR) vesicles, highlighting the broad utility of FQD probes. We thus establish that FQD probes exhibit excellent performance in single-molecule and live-cell imaging, and anticipate that they could be widely adopted in many advanced imaging techniques that rely on photoactivation.

Results

We designed two types of FQD that are bimolecular (FQD_2) and unimolecular (FQD_1) in structures. FQD_2 is comprised of two complementary oligo strands (**Fig. 1a**), in which one strand carries the fluorophore, e.g., Alexa Fluor 488, Alexa Fluor 594, and Alexa Flour 647 (AF488, AF594, and AF647, respectively), and the other carries the photocleavable linker (PC Linker) and the quencher, e.g., Black Hole Quencher 2 (BHQ2). Native polyacrylamide gel electrophoresis analysis confirmed the successful annealing of several different FQD_2 variants (**Supplementary Fig. 1a**). The close proximity between the fluorophore and quencher upon DNA annealing leads to the non-fluorescent "off" state of FQD_2. The current FQD_2 uses a 29-base-pair (bp) DNA scaffold, yielding a molecular weight around 20 kDa, similar to that of many protein-labeling tags. To achieve the minimal size of FQD, we also designed the unimolecular FQD_1 (**Fig. 1a**), whose fluorophore, PC Linker, and quencher are separated only by one-nucleotide (nt) spacers (i.e., effective molecular weight about 2.5 kDa). To measure the photoactivation kinetics of FQD, the fluorescence spectra of FQD_1 and FQD_2 were obtained before and after different time points of UV illumination (~0.03 W/cm^2) and compared to those of PA JF549 and PA JF646 treated under the same condition (**Supplementary Figs. 1b-g**). After UV illumination, gradual fluorescence recovery was observed for all PA probes; FQD became fully activated within 5–10 min, whereas PA JF549 and PA JF646 required a longer illumination of > 60 min and 30 min, respectively, indicating a faster kinetics of photoactivation for FQD (**Supplementary Fig. 1h**). We calculated the on-off intensity ratios of different PA probes and found that all FQD probes exhibited a > 100-fold intensity increase after photoactivation, with minimal residual fluorescence in the "off" state (**Supplementary Fig. 1h**).

To evaluate the performance of FQD in single-molecule imaging experiments, biotinylated $FQD_2$488 and $FQD_2$594 were immobilized on a surface via NeutrAvidin and biotinylated bovine serum albumin (BSA-biotin), and imaged with a confocal microscope (**Supplementary Fig. 2a**). The number of single-molecule spots increased after 405-nm illumination (**Supplementary Fig. 2b**), indicating the successful photoactivation of $FQD_2$488 and $FQD_2$594. The intensity trajectories of these molecules showed single activation and photobleaching steps, consistent with single fluorophores being observed (**Supplementary Figs. 2c,d**). To estimate the 405-nm laser intensity required for FQD activation, we titrated the input laser power setting on the microscope, and measured the percentage of photoactivated molecules after different illumination periods. At the 40–100% 405-nm laser powers (approximately 0.6 kW/cm^2 at 100% and for details see Methods), most $FQD_2$488 and $FQD_2$594 molecules were switched on within 5 frames of activation (with each frame corresponding to a single-molecule photoactivation time of 4.78 ms, **Supplementary Figs. 2e-h** and for details see Methods).

To further explore deep volumetric single-molecule imaging, the Acrydite-labeled Oligo A in $FQD_2$594 was formulated with acrylamide and bis-acrylamide monomers; upon mixing with the initiator ammonium persulfate (APS) and the catalyst tetramethylethylenediamine (TEMED), Acrydite-Oligo A-AF594 became cross-linked into a hydrogel (**Figs. 1b,c**). The PC Linker and BHQ2-containing Oligo B was then diffused into the hydrogel, resulting in the disappearance of single-molecule spots following the in situ hybridization between the two oligo strands (**Figs. 1b,d**). After 405-nm illumination, a recovery of the Acrydite-$FQD_2$594 spots was observed (**Figs. 1b,e**), indicating the successful photoactivation of Acrydite-$FQD_2$594 in 3D hydrogels. The signals of photoactivated Acrydite-$FQD_2$594 in 3D hydrogels were collected at varying imaging depths,

revealing a slight decrease in the SNR at an increasing depth. However, distinct single-molecule signals could still be detected at 13 μm (**Figs. 1f,g**), substantially surpassing the imaging depth achievable with TIRF and highly inclined and laminated optical sheet (HILO) microscopy.[26] Single-molecule photoactivation and observation of Acrydite-FQD$_2$594 were further confirmed by intensity trajectory analysis (**Fig. 1h,i**); a 20% 405-nm laser power achieved near-complete fluorophore recovery and was as effective for photoactivation as higher laser powers (**Figs. 1j,k**). Based on the results above, we validated the feasibility of single-molecule photoactivation and confocal imaging of FQD both on 2D surfaces and in 3D hydrogels.

Next, we tested if FQD can be used in confocal PhADE experiments (for details see Methods) to break the "concentration barrier". A high concentration of diffusing FQD$_2$594 (1 μM) was added in the solution to interfere with the detection of immobilized FQD$_2$594 on the surface (**Supplementary Fig. 3a**). During a PhADE cycle, both the immobilized and diffusing FQD$_2$594 molecules in the imaging volume were initially photoactivated; however, the non-immobilized FQD$_2$594 subsequently diffused out of the imaging volume, leading to a gradual increase in the SNR of the immobilized FQD$_2$594 molecules, so that the single-molecule signals were eventually detected (**Supplementary Figs. 3b,c**). Consistent with PhADE being a diffusion-dependent process, the decay of background fluorescence was hampered at an increased solution viscosity (25% vs. 0% glycerol, **Supplementary Fig. 3d**). This effect was further supported by the diffusion coefficients of FQD$_2$594 determined with fluorescence correlation spectroscopy (FCS), i.e., 113.498 ± 4.818 μm^2/s and 37.835 ± 2.502 μm^2/s in 0% and 25% glycerol, respectively (**Supplementary Figs. 3e,f**).

So far, the PhADE strategy has only been implemented with surface-proximal imaging. We applied the confocal PhADE method to image single Acrydite-FQD$_2$594 molecules tethered in 3D hydrogels in the presence of diffusing FQD$_2$594 (1 μM, **Fig. 2a**). Our results demonstrated a complete PhADE cycle in 3D hydrogels (at an imaging depth of 4 μm), where the recovery of SNR and the detection of single-molecule signals were achieved for the immobilized FQD$_2$594 molecules (**Figs. 2b,c** and **Supplementary Fig. 4**). Next, multiple PhADE cycles were strung for continuous observation (**Fig. 2d**), and the 1–2 frames at the end of each PhADE cycle were selected and concatenated post-data acquisition to generate a time-lapse dataset for downstream analysis (**Fig. 2e**), providing an effective time resolution equal to the duration of one PhADE cycle. The decay of background fluorescence followed a double-exponential model in hydrogels with time constants similar to that obtained on surfaces in aqueous solution (0.6 s and 4.0 s in hydrogels vs. 4.4 s on surfaces, **Fig. 2d** and **Supplementary Fig. 3d**). Based on the results above, we found that the confocal PhADE method could be implemented for breaking the "concentration barrier" in single-molecule fluorescence imaging both in 2D and 3D systems, which showed a minimal "dead time" thanks to the fast diffusion and dissipation process.

To demonstrate the utility of deep volumetric confocal PhADE, we applied this method to monitor the growth process of individual RCA products in hydrogels. To study RCA reactions in the hydrogel, we hybridized the Acrydite-labeled RCA primer with the circular RCA template, and copolymerized the complex with the hydrogel. For monitoring RCA reactions in real time, we designed a hybridization probe complementary to the RCA product and labeled the probe with FQD$_2$594 (RCA probe-FQD$_2$594). RCA reactions were initiated by adding phi29 DNA Polymerase and dNTPs in the buffer that soaks the hydrogel. As the reaction proceeded, each amplification cycle generated a binding site for RCA probe-FQD$_2$594, resulting in a progressive increase in fluorescence intensity (**Fig. 2f**). At the 2.5 μM probe concentration, individual RCA reactions could barely be

imaged with the regular AF594-labeled hybridization probe (RCA probe-AF594) because of an overwhelming background fluorescence (**Fig. 2g**). In comparison, clear visualization and tracking of single RCA reactions were allowed with RCA probe-$FQD_2$594 when imaged with the deep volumetric confocal PhADE method under the identical probe concentration and imaging conditions (**Fig. 2h** and **Supplementary Fig. 5**). This approach enabled real-time visualization of individual RCA reactions even at 10 μm above the imaging surface. We extracted the fluorescence intensity trajectories and analyzed the growth curves for individual RCA reactions (**Fig. 2i**). Most trajectories displayed a biphasic profile, with an initial steep phase followed by a slower, more gradual one (**Supplementary Fig. 6**). To understand how these trajectories reflect the underlying RCA reaction kinetics, we simulated the reaction and photoactivation processes with different parameters. The first phase was found to reflect contributions from both the reaction and photoactivation processes, while the slope of the second phase was more closely correlated with the reaction kinetics (**Supplementary Fig. 6e**).

To further test if deep volumetric confocal PhADE can detect signals from single fluorophores, we utilized DNA hybridization in hydrogels as the model system. To measure the DNA hybridization kinetics in hydrogels, we anchored the Acrydite-AF488-docking strands during polymerization, and added the complementary $FQD_1$594-imager strands via diffusion (**Fig. 3a**). A volumetric confocal reconstruction revealed the spatial distribution of the Acrydite-AF488-docking strands throughout the hydrogel matrix (**Fig. 3b**). We acquired single-molecule images from two color channels, and the co-localization analysis confirmed the specific interaction between the $FQD_1$594-imager strands and the immobilized Acrydite-AF488-docking strands (**Fig. 3c**). Notably, at an imager strand concentration of 100 nM, conventional confocal microscopy of the imager strands labeled with regular AF594 failed to visualize single-molecule spots due to the high background fluorescence (**Fig. 3d**, top). In contrast, deep volumetric confocal PhADE detected single-molecule signals of the $FQD_1$594-imager strands at the identical probe concentration and imaging conditions, displaying distinct unoccupied and hybridized states in the representative fluorescence intensity trajectory (**Fig. 3d**, bottom). Even at an imager strand concentration of 200 nM, clear single-molecule steps could be observed (**Supplementary Fig. 7a**), indicating that 1 frame of 0.52 s is sufficient for diffusion and background fluorescence dissipation in hydrogels at this imager strand concentration.

By monitoring these individual events in real time at varying imager strand concentrations, the hybridization kinetic parameters within the hydrogel were characterized. The dissociation rate (k_{off}) was calculated from the mean bound dwelltime (τ_b) to be approximately 0.06 s^{-1}, independent of the imager strand concentration (**Fig. 3e**), whereas the apparent association rate (k_{on}) was derived from the mean unbound dwelltime (τ_d), exhibiting a dependence on the imager strand concentration. Interestingly, as the imager strand concentration increased, the observed k_{on} increased and reached a plateau at 50 nM (**Fig. 3f**). This is likely due to a portion of the imager strands being unlabeled or photobleached; the 10-nt complementarity and therefore long bound dwelltimes of these non-fluorescent imager strands can substantially affect the measured unbound dwelltimes when misinterpreted as unbound events (**Supplementary Fig. 7b**). This artifact can be mitigated if a faster-dissociation imager strand is used in combination with a faster imaging modality (**Supplementary Fig. 7c**).

Owing to their DNA scaffolds, FQD probes can be readily integrated with DNA aptamers to extend their applications to live-cell imaging. We selected an aptamer against the CI-M6PR,[27, 28] a transmembrane receptor that cycles between the plasma membrane and intracellular

compartments, and extended its 5′ end to included FQD_2647 (M6PR aptamer-FQD_2647, **Fig. 4a**). Upon receptor binding, M6PR aptamer-FQD_2647 was endocytosed with the CI-M6PR vesicles; both whole-cell and localized photoactivation switched on the internalized FQD_2647 (**Fig. 4b**), enabling visualization and tracking of individual CI-M6PR vesicles in live cells (**Fig. 4c**). To quantify vesicle mobility, we performed mean square displacement (MSD) analysis and obtained a median diffusion coefficient (D) of 0.0019 $\mu m^2/s$ from individual vesicles, comparable to the value from linear fitting of the averaged MSD vs. time lag curve (0.0041 $\mu m^2/s$, **Fig. 4d**).

Discussion

In this study, we synthesized a series of FQD probes with different colors, attachment groups, and scaffold structures. Our results showed that FQD probes can be photoactivated under modest UV illumination with an efficiency exceeding that of some commercial PA fluorophores (**Supplementary Fig. 1**). Regardless of the fluorophores and DNA structures tested, all FQD probes exhibited a high on-off intensity ratio (> 100-fold) and nearly uniform photoactivation kinetics, speaking to the advantage of its modular architecture. In comparison, BODIPY-based and 2,6-dinitrobenzyl-caged PA fluorophores exhibit deteriorating on-off intensity ratios at the yellow and red fluorescence wavelength.[3] Moreover, single-molecule photoactivation and imaging of FQD both on 2D surfaces (**Supplementary Fig. 2**) and in 3D hydrogels (**Fig. 1**) were demonstrated with a confocal microscope. Despite that the SNR slightly decreased as the imaging depth increased in hydrogels, we were able to perform single-molecule detection at 13 μm from the surface (**Figs. 1f,g**). FQD can be ordered with the fluorophore and quencher-of-choice, or as the unlabeled amino form, which can be easily conjugated in small batches in house (for details see Methods), making them accessible and flexible for various application scenarios.

Thanks to the unique advantages of FQD, we utilized the probes to expand the capabilities of several photoactivation-based imaging techniques. For instance, combining PhADE with confocal microscopy, we were able to overcome the "concentration barrier" in single-molecule fluorescence imaging both in 2D (**Supplementary Fig. 3**) and 3D systems (**Figs. 2a-e**), where the target single molecules were tethered on surfaces and in hydrogels, respectively. Single-molecule in vitro imaging experiments typically depends on functionalized and passivated surfaces for tethering target molecules for long-term observation.[29-32] Here, the hydrogel matrix is employed to immobilize the reaction systems, i.e., RCA (**Figs. 2f-i**) and DNA hybridization (**Fig. 3**), for continuous single-molecule monitoring, offering a practical alternative that could circumvent the relatively lengthy surface preparation steps. The non-specific binding level of DNA is minimal in hydrogels, as we did not observe single-molecule signals at an imager strand concentration of 100 nM when the docking strand is absent (**Supplementary Fig. 7d**).

One of the drawbacks of the current confocal PhADE method is the limited imaging speed. For instance, as a trade-off for a relatively large field of view in the RCA experiments, we shortened the pixel dwelltime to 9.75 μs but only achieved a modest time resolution of 4.1 s, comprising of 1.3 s of photoactivation and 2.6 s of diffusion and excitation (**Figs. 2g,h**). However, for a typical phi29 DNA Polymerase (50–100 nt/s), it takes about 1–1.5 s to amplify a 70-nt template, rendering the time resolution inadequate for observing step-wise intensity changes. In addition, while the shortened pixel dwelltime prevents detector saturation at high RCA probe-AF594 concentrations, it also reduces the SNR and makes it difficult to discern single-fluorophore intensity changes out of a large random noise from the RCA reaction spots containing tens of hybridized probes. The overall

imaging speed can be increased by adopting faster imaging modalities, such as spinning-disk confocal microscopy.[33]

In this study, FQD probes were integrated with the M6PR aptamer to track single-vesicle movement in live cells (**Fig. 4**). Its compatibility with aptamer-based affinity reagents, such as SOMAmers,[34, 35] could facilitate sptPALM[6] tracking of high-density surface receptors.[36] Moreover, incorporating FQD and PhADE in DNA point accumulation for imaging in nanoscale topography (DNA-PAINT)[37, 38] could suppress background fluorescence from high concentrations of imager strands required for efficient hybridization in hydrogel-embedded and cleared samples,[39] resulting in improved localization precision and imaging speed compared to conventional fluorophore-labeled imager strands (**Fig. 5a**). Alternatively, changing the transient probes to stable ones, one could utilize the photoactivatable FQD probes to perform PALM imaging in fixed cells (**Fig. 5b**). In summary, these FQD probes are readily accessible, versatile, and exhibit improved performance, which could facilitate a broad range of photoactivation-based imaging methods.

Methods

Materials

Sample chambers were ordered from Cellvis (C18SB-1.5H). HEPES solution (Sigma-Aldrich, 83264), Tris-HCl (pH 8.0, Beyotime, ST786), PBS (pH 7.4, Beyotime, ST476), potassium chloride (Aladdin, P112133), magnesium chloride (Sigma-Aldrich, 442615), EDTA (ThermoFisher, AM9260G), glucose (Sigma-Aldrich, G7528), (+-)-6-hydroxy-2,5,7,8-tetra-methylchromane-2-carboxylic acid (Trolox, Sigma-Aldrich, 238813), glucose oxidase (Sigma-Aldrich, G2133), catalase (Sigma-Aldrich, C9322), Alconox (Sigma-Aldrich, Z742914), potassium hydroxide (Sigma-Aldrich, 484016), BSA (Sigma-Aldrich, A1933), biotin-PEG3 NHS ester (MCE, 130291), ultrafiltration spin columns (10 kDa, Beyotime, FUF051), Tween 20 (Sigma-Aldrich, T8787), NeutrAvidin (Thermo Scientific, 31000), triethoxyvinylsilane (Sigma-Aldrich, 679275), ethanol (Aladdin, E111993), acetic acid (Aladdin, A298827), 40% acrylamide-bisacrylamide (19:1) (Beyotime, ST004B), APS (Sigma-Aldrich, A3678), TEMED (Sigma-Aldrich, T7024), glycerol (Sigma-Aldrich, G5516), AF594 NHS ester (Lumiprobe, 2825), AF647 NHS ester (MCE, HY-D1119), PA JF549 NHS ester (MCE, HY-133536), PA JF646 NHS ester (MCE, HY-133535), DMSO (Sigma-Aldrich, 276855), sodium bicarbonate (Aladdin, M0113576), Oligo Clean & Concentrator (OCC, Zymo Research, D4060), CircLigase II (Lucigen, CL9021K), phi29 DNA Polymerase (Beyotime, D7053S), DL500 DNA Marker (Takara, 3590Q), HEPES-free, high-glucose Dulbecco's modified Eagle's medium (DMEM, Sangon, E600002-0500), 10% fetal bovine serum (FBS, Vazyme, F101-01), penicillin-streptomycin (MCE, HY-K1006), live-cell imaging solution (ThermoFisher, A59688DJ).

Buffers

Buffer A was 25 mM HEPES, pH 7.6, 150 mM KCl, ultrapure H_2O.

Buffer B was 50 mM HEPES pH 7.6, 150 mM KCl, 0.8% glucose, 4 mM Trolox, ultrapure H_2O, and 1X Gloxy (165 U/mL glucose oxidase and 2170 U/mL catalase) was added before imaging.[40]

Buffer C was 5 mM Tris-HCl pH 8.0, 75 mM $MgCl_2$, 0.05% Tween-20, 1 mM EDTA, 0.8% glucose, 4 mM Trolox, ultrapure H_2O, and 1X Gloxy was added before imaging.[40, 41]

Buffer D was 1 U phi29 DNA Polymerase, 0.25 mM dNTPs, 1X RCA reaction buffer, 0.8% glucose, 4 mM Trolox, ultrapure H_2O, and 1X Gloxy was added before imaging.[40]

Buffer E was 25 mM HEPES, pH 7.6, 150 mM KCl, 0.2% Tween 20, ultrapure H_2O.

Oligonucleotide preparation

Oligo A-AF488/594, Acrydite-Oligo A-amino, Oligo B, Oligo B-biotin, Oligo C-amino, P-Oligo D, Oligo E-Acrydite, $FQD_1$594-imager strand, Acrydite-AF488-docking strand (10 nt), Acrydite-docking strand (8 nt), AF488-docking strand-biotin, M6PR aptamer A-amino, M6PR-aptamer B, and other oligos were purchased from Sangon Biotech.

Acrydite-Oligo A-AF594 was labeled in house. Specifically, Acrydite-Oligo A-amino was mixed with AF594 NHS ester in $NaHCO_3$ buffer at a 50-fold molar excess for 3 h at room temperature. Acrydite-Oligo A-AF594 was then purified with OCC. The labeling efficiency was determined by UV-absorbance using NanoDrop.

Oligo C-AF594 and Oligo C-AF647 were labeled in house. Specifically, Oligo C-amino was mixed with AF594 and AF647 NHS ester in $NaHCO_3$ buffer at a 50-fold molar excess for 3 h at room temperature, respectively. Oligo C-AF594 and Oligo C-AF647 were then purified with OCC. The labeling efficiency was determined by UV-absorbance using NanoDrop.

M6PR aptamer A-AF647 was labeled in house. Specifically, M6PR aptamer A-amino was mixed with AF647 NHS ester in $NaHCO_3$ buffer at a 50-fold molar excess for 3 h at room temperature. M6PR aptamer A-AF647 was then purified with OCC. The labeling efficiency was determined by UV-absorbance using NanoDrop.

$FQD_2$488/594 ($FQD_2$488/594-biotin) was synthesized by hybridizing Oligo A-AF488/AF594 with Oligo B (Oligo B-biotin). Acrydite-$FQD_2$594 was synthesized by hybridizing Acrydite-Oligo A-AF594 with Oligo B. RCA probe-$FQD_2$594 and $FQD_2$647 were synthesized by hybridizing Oligo C-AF594 and Oligo C-AF647 with Oligo B, respectively. Acrydite-AF488-docking strand-biotin (8 nt) was synthesized by hybridizing Acrydite-docking strand (8 nt) with AF488-docking strand-biotin. M6PR aptamer-$FQD_2$647 was synthesized by hybridizing M6PR aptamer A-AF647 with M6PR-aptamer B.

P-Oligo D was ligated into a circular form using the CircLigase II kit. The circularized Oligo D was purified with OCC. The Acrydite-labeled RCA primer (Oligo E-Acrydite, 10 μM) and the circular RCA template were mixed for hybridization in Buffer A, and the hybridized RCA initiation complex was purified with OCC.

DNA hybridization was carried out by heating samples to 95 °C for 5 min, followed by slow cooling to 30 °C in approximately 10 min in Buffer A. Native polyacrylamide gel electrophoresis analysis (10%) was used to examine DNA hybridization. All oligo samples were stored at -20 °C.

Bulk photoactivation assays and fluorescence spectrometry

The samples were diluted in buffer A at a concentration of 200 nM and illuminated with a UV LED lamp at a fixed angle and distance for the specified time periods. The UV illumination intensity was measured with a power meter with the lamp held at the same fixed angle and distance. All fluorescence spectra were measured on a Carry Eclipse (Agilent) fluorometer. For $FQD_2$488, the excitation wavelength was 480 nm and the emission wavelength window was 500–600 nm. For $FQD_2$594 and $FQD_1$594, the excitation wavelength was 580 nm and the emission wavelength window was 600–700 nm. For $FQD_2$647 and PA JF646, the excitation wavelength was 640 nm and the emission wavelength window was 660–760 nm. For PA JF549, the excitation wavelength was 540 nm and the emission wavelength window was 560–660 nm. The excitation and emission slit width was 10 nm, and the scan speed was 600 nm/min. A photomultiplier tube was used as the detector.

Imaging surface preparation

The potassium hydroxide-treated imaging surface was prepared by the sequential sonication steps as follows: glass slides and coverslips were first sonicated in 0.5% (w/v) Alconox solution for 20 min, then in ultrapure H_2O for 5 min, and in 2 M KOH solution for 20 min. The slides were then thoroughly washed with ultrapure H_2O and dried with nitrogen gas. The treated slides and coverslips were assembled into imaging channels before experiments.

For the triethoxyvinylsilane-modified imaging surface, imaging chambers were cleaned and KOH-treated following the same procedure described above. The chambers were then subjected to oxygen plasma treatment (80 W, 5 min), followed by overnight incubation at room temperature in 0.3% acetic acid, 0.2% triethoxyvinylsilane and 95% ethanol. Finally, the imaging chambers were rinsed with absolute ethanol and dried with nitrogen gas.

Confocal microscopy

The single-molecule imaging experiments were performed on a Leica TCS SP8 STED microscope or a Leica Stellaris 8 STED microscope that is equipped with a 405-nm laser, a white light laser (WLL) source, and an HC PL APO CS2 100× or 63× oil-immersion objective (NA = 1.4). All confocal PhADE experiments were performed in the fluorescence recovery after photobleaching (FRAP) mode.

AF488, AF594, and AF647 were excited with the 488-nm, 580-nm, and 647-nm lasers, respectively, from the WLL source. Fluorescence emission was collected in the photon-counting mode (gate time 0.3–6.0 ns) with wavelength windows of 500–600 nm (for AF488), 600–700 nm (for AF594), and 670–770 nm (for AF647) using a HyD detector. The laser power, scanning speed, pixel size, image size, and z-depth were specified in the figure captions for each experiment.

The photoactivation time per molecule was estimated from the 405-nm illumination duration during confocal scanning of 7×7 pixels. For example, based on the pixel dwelltime of 97.65 μs and pixel size of 53.84 nm, the calculated photoactivation time per molecule was 4.78 ms per frame (Leica TCS SP8 STED microscope). For the pixel dwelltime of 102.38 μs and pixel size of 51.53 nm, the calculated photoactivation time per molecule was 5.01 ms per frame (Leica Stellaris 8 STED microscope). The effective diffusion time in a PhADE cycle was derived from the time interval between the two consecutive confocal scans of the same molecule.

The 405-nm laser intensity at each input laser power setting was measured with a power meter held after the objective. The 405-nm laser power density was estimated with an assumed focal spot size of 350 × 350 nm^2.

Surface-proximal confocal PhADE

BSA-biotin was custom synthesized with BSA and biotin-PEG3 NHS ester. Specifically, biotin-PEG3 NHS ester was added to BSA in a large molar excess and the mixture was incubated at room temperature overnight. The excess biotin-PEG3 NHS ester was removed with ultrafiltration spin columns.

50 μL of 0.2 mg/mL BSA-biotin was introduced to an imaging channel and incubated for 20 min, followed by a wash with 100 μL of Buffer E. Next, 50 μL of 0.1 mg/mL NeutrAvidin was added and incubated for 20 min, and the channel was washed with 100 μL of Buffer A. 100 μL of 1 nM $FQD_2$488/594-biotin was then added and incubated for 5 min, followed by another wash with Buffer A. Finally, 1 μM $FQD_2$488/594 was introduced to the channel in Buffer B containing 1X Gloxy.

Surface-proximal confocal PhADE was carried on a confocal microscope (see confocal microscopy). This process includes the photoactivation (405 nm) and excitation (488 nm or 594 nm) steps. For each experiment, the detailed imaging parameters are shown in the corresponding figure captions.

Deep volumetric confocal PhADE

A pre-hydrogel solution (5 μL) was first prepared by mixing 2% acrylamide-bisacrylamide (19:1), Acrydite-Oligo A-AF594 (6 nM), and ultrapure H_2O. Subsequently, 0.1% APS and 1X TEMED were added sequentially. The mixture was gently pipetted up and down three times and immediately added into a triethoxyvinylsilane-functionalized imaging chamber. All the preparation steps were performed on ice until polymerization. After polymerization, the chamber was washed three times with 300 μL of 1X PBS buffer (2 min per wash). Next, 100 μL of Oligo B (5 nM) was

added onto the hydrogel and allowed to hybridize overnight at 4 °C. Following hybridization, the hydrogel was washed three times with 300 μL of 1X PBS buffer (2 min per wash). Finally, 1 μM $FQD_2$594 was introduced to the chamber in Buffer B containing 1X Gloxy.

Deep volumetric confocal PhADE was carried on a confocal microscope (see confocal microscopy). This process includes the photoactivation (405 nm) and excitation (594 nm) steps. For each experiment, the detailed imaging parameters are shown in the corresponding figure captions.

Deep volumetric confocal PhADE imaging of individual RCA reactions

A pre-hydrogel solution (5 μL) was first prepared by mixing 3% acrylamide-bisacrylamide (19:1), the RCA initiation complex (125 nM), and ultrapure H_2O. Subsequently, 0.2% APS and 10X TEMED were added sequentially. The mixture was gently pipetted up and down three times and immediately added into a triethoxyvinylsilane-functionalized imaging chamber. All the preparation steps were performed on ice until polymerization. After polymerization, the chamber was washed three times with 300 μL of 1X PBS buffer (2 min per wash). Next, 1X RCA reaction buffer (from phi29 DNA Polymerase, Beyotime, D7053S) containing RCA probe-$FQD_2$594 or RCA probe-AF594 (2.5 μM) were added into the hydrogel that was already copolymerized with the RCA initiation complex and incubated on ice for 10 min. The RCA reaction mixture was prepared on ice by combining phi29 DNA Polymerase (1 U), dNTPs (250 μM), 1X RCA reaction buffer, the oxygen-scavenging system components (0.8% glucose, 4 mM Trolox), and 1X Gloxy. The real-time imaging of RCA reactions was carried out by the deep volumetric confocal PhADE method (see confocal microscopy and deep volumetric confocal PhADE).

Simulation of the reaction and photoactivation processes

The time duration for each RCA cycle was simulated by a Gamma random number function in MatLab (steps = 70 nt, time per step = 1/phi29 DNA Polymerase speed). Since the RCA probe was at a high concentration, its binding was considered instantaneous. At each photoactivation frame, the number of newly photoactivated probes was simulated by a normal random number function in MatLab (mean = the number of dark probes × photoactivation efficiency, standard deviation = √mean). The number of total photoactivated probes was the cumulative sum of the number of newly photoactivated probes, without considering photobleaching. Various combinations of phi29 DNA Polymerase speed and photoactivation efficiency were simulated.

Deep volumetric confocal PhADE imaging of single DNA hybridization events

A pre-hydrogel solution (5 μL) was first prepared by mixing 2% acrylamide-bisacrylamide (19:1), the Acrydite-AF488-docking strand (6 nM), and ultrapure H_2O. Subsequently, 0.1% APS and 1X TEMED were added sequentially. The mixture was gently pipetted up and down three times and immediately added into a triethoxyvinylsilane-functionalized imaging chamber. All the preparation steps were performed on ice until polymerization. After polymerization, the chamber was washed three times with 300 μL of 1X PBS buffer (2 min per wash). Next, the $FQD_1$594-imager strands (10, 20, 50, 100, 200 nM) in Buffer C were incubated with the hydrogel for 1 h before 1X Gloxy was added. The real-time imaging of DNA hybridization events was carried out by the deep volumetric confocal PhADE imaging method (see confocal microscopy and deep volumetric confocal PhADE).

Simulation of the apparent association rate

The Gillespie method was performed to simulate τ_b and τ_d dwelltimes, given the specified dissociation rate (k_{off}) and association rate (k_{on}). To mimic the effect of non-fluorescent imager strands, a portion of the bound events, specified by the labeling efficiency, were randomly selected and merged with the neighboring unbound events. The apparent dissociation rate and association rate were calculated from the mean τ_b and τ_d dwelltimes, respectively, after considering that a portion of bound events were misinterpreted as unbound events.

Cell Culture and live-cell imaging

MCF-7 cells were cultured in HEPES-free, high-glucose DMEM supplemented with 10% fetal bovine serum and 1X penicillin-streptomycin, and maintained in a humidified incubator at 37 °C with 5% CO_2. The cells were seeded in an 18-well glass-bottom chamber at a density of 2×10^4 cells per well. Following cell adhesion, the cells were incubated with 100 μL of M6PR aptamer-FQD_2647 (2.5 μM) at 37 °C for 2 h. After incubation, the cells were washed with 1X PBS and imaged in live-cell imaging solution to minimize background fluorescence. The real-time tracking of CI-M6PR vesicles was carried out in the FRAP mode on the Leica TCS SP8 STED microscope (see confocal microscopy).

Data analysis

All images were processed by custom-made scripts in MatLab. For background subtraction, a background image for each image was generated with a 7×7-pixel tiling-window median value, interpolation and smoothing algorithm. For single-molecule selection, signal spots were selected with a local maximum method with three exclusion criteria, i.e., if a spot was 1) too large, 2) too close to another spot, or 3) too close to the edge of the image, it was excluded for analysis. For single-molecule intensity extraction, the 7×7-pixel intensities centered around each selected single molecule were background-subtracted and summed with a Gaussian-weighted method (FWHM ~3 pixels). The noise and background values were calculated as the standard deviation and average of pixel intensities, respectively, from imaging regions where no spots were detected.

Single-vesicle tracking were performed with TrackMate in ImageJ. Spot detection employed a Laplacian-of-Gaussian (LoG) detector with median filtering for pre-processing and sub-pixel localization (estimated object diameter 0.6 μm and quality threshold 1.0). Vesicle tracking used a Simple LAP tracker (linking maximum distance 2.0 μm, gap-closing maximum distance 1.0 μm, and gap-closing maximum frame gap 1 frame). Mean square displacements from tracks longer than 7 frames were used to determine the diffusion coefficient.

Table 1 The Oligo list.

Names	Sequences (5' to 3') and modifications
Oligo A strands	**Oligo A-AF488/594** CTCTATTTTGACTATATTTGACCTTAATC-AF488/594 **Acrydite-Oligo A-amino** Acrydite-CTCTATTTTGACTATATTTGACCTTAATC-NH_2
Oligo B strands	**Oligo B** BHQ2-GA/iPCLink/TTAAGGTCAAATATAGTCAAAATAGAG **Oligo B-biotin** BHQ2-GA/iPCLink/TTAAGGTCAAATATAGTCAAAATAGAG-biotin
Oligo C strands	**Oligo C-amino** CACCATAACATACCACTTTGATCTCTATTTTGACTATATTTGACCTTAATC-NH_2
Oligo D strands	**P-Oligo D** P-CCTATCTACATCACCCCAATCACCATAACATACCACTTTGACAATAACACACTCTC AACACCACCTACCA
Oligo E strands	**Oligo E-Acrydite** GGTGATGTAGATAGGTGGTAGGTGGTGTT-Acrydite
imager strands	**FQD$_1$594-imager strand** BHQ2/T/iPCLink/T/iAF594dT/TTCTAGATGTAT
docking strands	**Acrydite-AF488-docking strand (10 nt)** Acrydite-ATCCC/iAF488dT/ATCTTATACATCTAG **Acrydite-docking strand (8 nt)** Acrydite-CTTTTCTTCTTTTCTTTCTTTTCCTCCTCATACATCT **AF488-docking strand-biotin** AAGAAAGAAAAGAAGAAAAGT/iAF488dT/TT-biotin
aptamer strands	**M6PR aptamer A-amino** NH_2-TGCTTGCCAGTGATTGATCCAGGGCGCGTAGATGACGAGCAGTCCTAACAT CGTTTAGGAC **M6PR-aptamer B** TGGATCAATCACTGGCAAGCA/iPCLink/AG-BHQ2

Acknowledgments

We thank all members of the Boyang Hua group for helpful discussion. Besides, we acknowledge and thank Dr. Yi Shi and Dr. Weikang Wang at the School of Chemistry and Molecular Engineering, East China Normal University and Dr. Yin Ding at the School of Chemistry, Nanjing University, respectively, for providing the confocal microscopes used in this study and related technical support. This work was supported by the National Natural Science Foundation of China (Nos. 22404079, U24A20503), the Fundamental Research Funds for the Central Universities 2024300410, and the State Key Laboratory of Analytical Chemistry for Life Science, Nanjing University 5431ZZXM2403.

Author contributions

H.T.: Methodology, Investigation, Formal analysis, Writing–Original Draft, Writing–Review & Editing;

S.L.: Methodology, Investigation, Formal analysis, Writing–Original Draft, Writing–Review & Editing;

X.Z.: Investigation;

C.K.: Investigation;

X.X.: Writing–Original Draft, Writing–Review & Editing, Supervision, Funding acquisition;

B.H.: Conceptualization, Methodology, Writing–Original Draft, Writing–Review & Editing, Supervision, Funding acquisition

Conflict of interests

The authors declare no competing financial interest.

Data availability

The data supporting the findings of this study are available from the corresponding authors upon request.

References

(1) Loveland, A. B.; Habuchi, S.; Walter, J. C.; van Oijen, A. M. A general approach to break the concentration barrier in single-molecule imaging. Nat Methods 2012, 9 (10), 987–992.

(2) Peng, S.; Sun, R.; Wang, W.; Chen, C. Single-molecule photoactivation FRET: A general and easy-to-implement approach to break the concentration barrier. Angew Chem Int Ed Engl 2017, 56 (24), 6882–6885.

(3) Ye, R.; Sun, X.; Mao, X.; Alfonso, F. S.; Baral, S.; Liu, C.; Coates, G. W.; Chen, P. Optical sequencing of single synthetic polymers. Nat Chem 2024, 16 (2), 210–217.

(4) Betzig, E.; Patterson, G. H.; Sougrat, R.; Lindwasser, O. W.; Olenych, S.; Bonifacino, J. S.; Davidson, M. W.; Lippincott-Schwartz, J.; Hess, H. F. Imaging intracellular fluorescent proteins at nanometer resolution. Science 2006, 313 (5793), 1642–1645.

(5) Hess, S. T.; Girirajan, T. P.; Mason, M. D. Ultra-high resolution imaging by fluorescence photoactivation localization microscopy. Biophys J 2006, 91 (11), 4258–4272.

(6) Manley, S.; Gillette, J. M.; Patterson, G. H.; Shroff, H.; Hess, H. F.; Betzig, E.; Lippincott-Schwartz, J. High-density mapping of single-molecule trajectories with photoactivated localization microscopy. Nat Methods 2008, 5 (2), 155–157.

(7) Li, D.; Shao, L.; Chen, B. C.; Zhang, X.; Zhang, M.; Moses, B.; Milkie, D. E.; Beach, J. R.; Hammer, J. A., 3rd; Pasham, M.; et al. Advanced imaging. Extended-resolution structured illumination imaging of endocytic and cytoskeletal dynamics. Science 2015, 349 (6251), aab3500.

(8) Balzarotti, F.; Eilers, Y.; Gwosch, K. C.; Gynnå, A. H.; Westphal, V.; Stefani, F. D.; Elf, J.; Hell, S. W. Nanometer resolution imaging and tracking of fluorescent molecules with minimal photon fluxes. Science 2017, 355 (6325), 606–612.

(9) Zou, Z.; Luo, Z.; Xu, X.; Yang, S.; Qing, Z.; Liu, J.; Yang, R. Photoactivatable fluorescent probes for spatiotemporal-controlled biosensing and imaging. TrAC Trends in Analytical Chemistry 2020, 125, 115811.

(10) Zhang, L.; Shen, D.; Yang, J. Advancing single-molecule biophysics: Next-generation organic fluorophores with tailored labeling strategies. Chem Biomed Imaging 2025, 3 (9), 572–598.

(11) Holzmeister, P.; Acuna, G. P.; Grohmann, D.; Tinnefeld, P. Breaking the concentration limit of optical single-molecule detection. Chem Soc Rev 2014, 43 (4), 1014–1028.

(12) White, D. S.; Smith, M. A.; Chanda, B.; Goldsmith, R. H. Strategies for overcoming the single-molecule concentration barrier. ACS Meas Sci Au 2023, 3 (4), 239–257.

(13) Patterson, G. H.; Lippincott-Schwartz, J. A photoactivatable GFP for selective photolabeling of proteins and cells. Science 2002, 297 (5588), 1873–1877.

(14) Lippincott-Schwartz, J.; Patterson, G. H. Photoactivatable fluorescent proteins for diffraction-limited and super-resolution imaging. Trends Cell Biol 2009, 19 (11), 555–565.

(15) Jang, S.; Kim, M.; Shim, S. H. Reductively caged, photoactivatable DNA-PAINT for high-throughput super-resolution microscopy. Angew Chem Int Ed Engl 2020, 59 (29), 11758–11762.

(16) Lincoln, R.; Bossi, M. L.; Remmel, M.; D'Este, E.; Butkevich, A. N.; Hell, S. W. A general design of caging-group-free photoactivatable fluorophores for live-cell nanoscopy. Nat Chem 2022, 14 (9), 1013–1020.

(17) Tang; Dmochowski, I. J. Phototriggering of caged fluorescent oligodeoxynucleotides. Organic Letters 2005, 7 (2), 279–282.

(18) Maurel, D.; Banala, S.; Laroche, T.; Johnsson, K. Photoactivatable and photoconvertible fluorescent probes for protein labeling. ACS Chem Biol 2010, 5 (5), 507–516.

(19) Friedrich, F.; Klehs, K.; Fichte, M. A. H.; Junek, S.; Heilemann, M.; Heckel, A. A two-photon activatable amino acid linker for the induction of fluorescence. Chemical Communications 2015, 51 (84), 15382–15385.
(20) Aktalay, A.; Khan, T. A.; Bossi, M. L.; Belov, V. N.; Hell, S. W. Photoactivatable carbo- and silicon-rhodamines and their application in MINFLUX nanoscopy. Angew Chem Int Ed Engl 2023, 62 (41), e202302781.
(21) Grimm, J. B.; English, B. P.; Choi, H.; Muthusamy, A. K.; Mehl, B. P.; Dong, P.; Brown, T. A.; Lippincott-Schwartz, J.; Liu, Z.; Lionnet, T.; et al. Bright photoactivatable fluorophores for single-molecule imaging. Nat Methods 2016, 13 (12), 985–988.
(22) Frei, M. S.; Hoess, P.; Lampe, M.; Nijmeijer, B.; Kueblbeck, M.; Ellenberg, J.; Wadepohl, H.; Ries, J.; Pitsch, S.; Reymond, L.; et al. Photoactivation of silicon rhodamines via a light-induced protonation. Nat Commun 2019, 10 (1), 4580.
(23) Platzer, R.; Rossboth, B. K.; Schneider, M. C.; Sevcsik, E.; Baumgart, F.; Stockinger, H.; Schütz, G. J.; Huppa, J. B.; Brameshuber, M. Unscrambling fluorophore blinking for comprehensive cluster detection via photoactivated localization microscopy. Nat Commun 2020, 11 (1), 4993.
(24) Niekamp, S.; Stuurman, N.; Vale, R. D. A 6-nm ultra-photostable DNA FluoroCube for fluorescence imaging. Nat Methods 2020, 17 (4), 437–441.
(25) Chu, J.; Ejaz, A.; Lin, K. M.; Joseph, M. R.; Coraor, A. E.; Drummond, D. A.; Squires, A. H. Single-molecule fluorescence multiplexing by multi-parameter spectroscopic detection of nanostructured FRET labels. Nature Nanotechnology 2024, 19 (8), 1150–1157.
(26) Tokunaga, M.; Imamoto, N.; Sakata-Sogawa, K. Highly inclined thin illumination enables clear single-molecule imaging in cells. Nat Methods 2008, 5 (2), 159–161.
(27) Li, Y.; Liu, X.; Yu, L.; Huang, X.; Wang, X.; Han, D.; Yang, Y.; Liu, Z. Covalent lytac enabled by DNA aptamers for immune checkpoint degradation therapy. Journal of the American Chemical Society 2023, 145 (45), 24506–24521.
(28) Zhang, R.; Yang, C.; Gao, X.; He, Z.; Ji, D.-K.; Tan, W. Phototriggered lytac: Photoactive bispecific aptamer chimera enhances targeted degradation of membrane protein through regulating cell autophagy. Journal of the American Chemical Society 2025, 147 (24), 20989–21002.
(29) Ha, T.; Rasnik, I.; Cheng, W.; Babcock, H. P.; Gauss, G. H.; Lohman, T. M.; Chu, S. Initiation and re-initiation of DNA unwinding by the Escherichia coli Rep helicase. Nature 2002, 419 (6907), 638–641.
(30) Hua, B.; Han, K. Y.; Zhou, R.; Kim, H.; Shi, X.; Abeysirigunawardena, S. C.; Jain, A.; Singh, D.; Aggarwal, V.; Woodson, S. A.; et al. An improved surface passivation method for single-molecule studies. Nat Methods 2014, 11 (12), 1233–1236.
(31) Broadwater, D. W. B.; Altman, R. B.; Blanchard, S. C.; Kim, H. D. ERASE: A novel surface reconditioning strategy for single-molecule experiments. Nucleic Acids Res 2019, 47 (3), e14.
(32) Paul, T.; Ha, T.; Myong, S. Regeneration of PEG slide for multiple rounds of single-molecule measurements. Biophys J 2021, 120 (9), 1788–1799.
(33) Schueder, F.; Lara-Gutiérrez, J.; Beliveau, B. J.; Saka, S. K.; Sasaki, H. M.; Woehrstein, J. B.; Strauss, M. T.; Grabmayr, H.; Yin, P.; Jungmann, R. Multiplexed 3D super-resolution imaging of whole cells using spinning disk confocal microscopy and DNA-PAINT. Nat Commun 2017, 8 (1), 2090.
(34) Gelinas, A. D.; Davies, D. R.; Edwards, T. E.; Rohloff, J. C.; Carter, J. D.; Zhang, C.; Gupta, S.; Ishikawa, Y.; Hirota, M.; Nakaishi, Y.; et al. Crystal structure of interleukin-6 in complex with a

modified nucleic acid ligand. Journal of Biological Chemistry 2014, 289 (12), 8720–8734.
(35) Rohloff, J. C.; Gelinas, A. D.; Jarvis, T. C.; Ochsner, U. A.; Schneider, D. J.; Gold, L.; Janjic, N. Nucleic acid ligands with protein-like side chains: Modified aptamers and their use as diagnostic and therapeutic agents. Molecular Therapy - Nucleic Acids 2014, 3, e201.
(36) Delcanale, P.; Porciani, D.; Pujals, S.; Jurkevich, A.; Chetrusca, A.; Tawiah, K. D.; Burke, D. H.; Albertazzi, L. Aptamers with tunable affinity enable single-molecule tracking and localization of membrane receptors on living cancer cells. Angewandte Chemie International Edition 2020, 59 (42), 18546–18555.
(37) Jungmann, R.; Steinhauer, C.; Scheible, M.; Kuzyk, A.; Tinnefeld, P.; Simmel, F. C. Single-molecule kinetics and super-resolution microscopy by fluorescence imaging of transient binding on DNA origami. Nano Lett 2010, 10 (11), 4756–4761.
(38) Strauss, S.; Nickels, P. C.; Strauss, M. T.; Jimenez Sabinina, V.; Ellenberg, J.; Carter, J. D.; Gupta, S.; Janjic, N.; Jungmann, R. Modified aptamers enable quantitative sub-10-nm cellular DNA-PAINT imaging. Nature Methods 2018, 15 (9), 685–688.
(39) Stein, J.; Magni, L.; Church, G. M. DNA-PAINT imaging with hydrogel imprinting and clearing. ACS Sens 2025, 10 (5), 3340–3346.
(40) Rasnik, I.; McKinney, S. A.; Ha, T. Nonblinking and long-lasting single-molecule fluorescence imaging. Nat Methods 2006, 3 (11), 891–893.
(41) Schueder, F.; Stein, J.; Stehr, F.; Auer, A.; Sperl, B.; Strauss, M. T.; Schwille, P.; Jungmann, R. An order of magnitude faster DNA-PAINT imaging by optimized sequence design and buffer conditions. Nat Methods 2019, 16 (11), 1101–1104.

Fig. 1 Deep volumetric single-molecule imaging of Acrydite-FQD$_2$594 immobilized within a hydrogel matrix. a, Structures of FQD$_1$ and FQD$_2$ probes. FQD$_2$ represents the bimolecular construct annealed of two complementary oligo strands, whereas FQD$_1$ denotes the unimolecular construct made of a single oligo strand. **b**, Preparation workflow of anchoring Acrydite-FQD$_2$594 in a polyacrylamide hydrogel during the polymerization process. **c-e**, Representative volumetric confocal reconstructions of FQD$_2$594 molecules revealing that Acrydite-Oligo A-AF594 is immobilized in the hydrogel matrix (**c**); subsequent hybridization with the PC Linker and BHQ2-modified Oligo B yields FQD$_2$594 in the non-fluorescent "off" state (**d**); upon photoactivation, the PC Linker undergoes cleavage and BHQ2 hence dissociates, converting FQD$_2$594 to the fluorescent "on" state (**e**). Images were acquired using the Z-Stack mode. The image size was 6.84 × 6.84 × 2.5 μm^3, with a Z-step size of 0.5 μm covering a Z-range of 2.0–4.5 μm (relative to the coverslip surface at 0 μm). Both hydrogel polymerization and oligo hybridization were conducted in 1X PBS buffer (pH 7.4). **f**, Confocal images of FQD$_2$594 at varying Z depths. The image size was 6.84 × 6.84 μm^2. **g**, Statistics of the SNR of FQD$_2$594 molecules across different imaging depths. 3 random imaging regions (6.84 × 6.84 μm^2) with 75–98 molecules were analyzed per Z depth. **h**, Representative single-molecule images of FQD$_2$594 before (BP) and after (AP) photoactivation. The imaging depth was 2 μm, and the image size was 3.42 × 3.42 μm^2. **i**, Single-molecule intensity trajectories corresponding to the specific spots (I, II) annotated in the images in **h**. **j**, Quantification of the average spot counts per imaging area before hybridization (BH), after hybridization/before photoactivation (AH/BP), and after photoactivation (AP). 5 random imaging regions (Z depth at 2 μm, 13.76 × 13.76 μm^2) were analyzed per condition. **k**, Quantification of the average spot counts of photoactivated FQD$_2$594 per imaging area at different 405-nm laser powers. 5 random imaging regions (Z depth at 2 μm, 13.76 × 13.76 μm^2) were analyzed per condition. For the above confocal experiments, a scanning speed of 97.65 μs/pixel and a pixel size of 53.84 × 53.84 nm^2 were used. Photoactivation of 1 frame (equivalent to a single-molecule activation time of 4.78 ms per frame) was performed using a 20% 405-nm laser power unless otherwise specified. Error bars, the standard deviation (SD). Scale bars, 1 μm. All the single-molecule images were obtained in Buffer B, and 1X Gloxy was added before imaging.

Fig. 2 Deep volumetric confocal PhADE imaging. a, Principle of deep volumetric confocal PhADE imaging. Acrydite-$FQD_2$594 is immobilized, while diffusing $FQD_2$594 is infused into the hydrogel. Upon photoactivation (405 nm), both the immobilized Acrydite-$FQD_2$594 and the diffusing $FQD_2$594 near the focal spot are converted to the "on" state. During excitation (580 nm), the non-immobilized $FQD_2$594 diffuses out of the imaging volume, leading to a time-dependent increase in the SNR of the immobilized Acrydite-$FQD_2$594. **b**, Deep volumetric confocal PhADE imaging of Acrydite-$FQD_2$594 immobilized in a hydrogel matrix with 1 μM diffusing $FQD_2$594 (one PhADE cycle). The imaging depth was 4 μm, and the image size was 3.42 × 3.42 μm^2. Each image represents an average of five raw frames, corresponding to the time periods (A1–A8) annotated in **c**. **c**, Time-dependent SNR for the immobilized Acrydite-$FQD_2$594 in a single PhADE cycle. "Point A" denotes the specific spot marked in **b**; "Average" represents the mean SNR over all identified spots (n = 9). For the confocal experiments in **a-c**, a scanning speed of 97.65 μs/pixel and a pixel size of 53.84 × 53.84 nm^2 were used. Photoactivation of 2 frames (equivalent to a single-molecule activation time of 4.78 ms per frame) was performed using a 20% 405-nm laser power in **a-c**. **d**, Intensity decay curves of background fluorescence in continuous PhADE cycles at 1 μM $FQD_2$594. The double-exponential decay time constants were 0.6 s and 4.0 s, respectively. For the confocal experiments in **d**, a scanning speed of 97.65 μs/pixel and a pixel size of 53.84 × 53.84 nm^2 were used. Photoactivation of 2 frames (equivalent to a single-molecule activation time of 4.78 ms per frame) was performed using a 20% 405-nm laser power in **d**. The duration of diffusion and excitation was 20 frames. **e**, Workflow and representative images of deep volumetric confocal PhADE imaging (continuous PhADE cycles). **f**, Workflow of observing individual RCA reactions in the hydrogel with deep volumetric confocal PhADE imaging. The RCA initiation complex, consisting of the Acrydite-labeled RCA primer and the circular RCA template, is copolymerized into the hydrogel network, followed by the infusion of RCA probe-$FQD_2$594. The RCA reaction is initiated by the addition of phi29 DNA Polymerase and dNTPs. As the reaction proceeds, each amplification cycle generates a binding site for RCA probe-$FQD_2$594, resulting in a progressive increase in fluorescence intensity. **g**, Deep volumetric confocal imaging of individual RCA reactions (without PhADE) at 2.5 μM RCA probe-AF594. The imaging depth was 10 μm, and the image size was 13.76 × 13.76 μm^2. Each image represents an average of two raw frames. **h**, Deep volumetric confocal PhADE imaging of individual RCA reactions at 2.5 μM RCA probe-$FQD_2$594 (continuous PhADE cycles). The imaging depth was 10 μm, and the image size was 13.76 × 13.76 μm^2. Each image represents an average of two raw frames. **i**, Fluorescence intensity trajectories representing the growth curves of individual RCA reactions. The addition of phi29 DNA Polymerase and dNTPs was at t = 0 s. 13 consecutive movies were obtained from different regions, with each movie consisting of 25 PhADE cycles. For the confocal experiments in **f-i**, a scanning speed of 9.75 μs/pixel and a pixel size of 53.84 × 53.84 nm^2 were used. Photoactivation of 1 frame (equivalent to a single-molecule activation time of 4.78 ms per frame) was performed using a 20% 405-nm laser power in **f-i**. The duration of diffusion and excitation was 2 frames (approximately 2.6 s). Scale bars, 1 μm. All the single-molecule images in **a-e** were obtained in Buffer B, and 1X Gloxy was added before imaging. All the single-molecule results in **f-i** were obtained in Buffer D, and 1X Gloxy was added before imaging.

Fig. 3 Deep volumetric confocal PhADE imaging of single DNA hybridization events. a, Workflow of observing single DNA hybridization events in the hydrogel with deep volumetric confocal PhADE imaging. The FQD_1594-labeled imager strands interact with the Acrydite-AF488-labeled docking strands in the hydrogel. **b**, A representative volumetric confocal reconstruction revealing that the Acrydite-AF488-docking strands are immobilized in the hydrogel matrix. Images were acquired using the Z-Stack mode. The image size was 6.84 × 6.84 × 5 μm^3, with a Z-step size of 1 μm covering a Z-range of 2.0–7.0 μm (relative to the coverslip surface at 0 μm). **c**, Co-localization analysis between the AF488 channel (left) and the FQD_1594 channel (middle), and the co-localized pixel positions (right). The imaging depth was 4 μm, and the image size was 2.42 × 2.42 μm^2. **d**, Representative intensity trajectories with the unbound or dissociated state (τ_d) and the bound state (τ_b). Comparison between the confocal mode (top) and the confocal PhADE mode (bottom). **e**, Rate of dissociation ($k_{off} = 1/\tau_b$) as a function of the FQD_1594-imager strand concentration. **f**, Rate of binding ($k_{on} = 1/\tau_d$) as a function of the FQD_1594-imager strand concentration. The mean dwelltimes were derived from 3 random groups with 92–259 and 70–194 events in **e,f**, respectively. For the above confocal experiments, a scanning speed of 102.38 μs/pixel and a pixel size of 51.53 × 51.53 nm^2 were used. Photoactivation of 1 frame (equivalent to a single-molecule activation time of 5.01 ms per frame) was performed using a 20% 405-nm laser power. The duration of diffusion and excitation was 1 frame (approximately 0.52 s). Error bars, the standard deviation (SD). Scale bars, 0.5 μm. All the single-molecule results were obtained in Buffer C, and 1X Gloxy was added before imaging.

Fig. 4 Live-cell tracking of individual CI-M6PR vesicles. a, Structure of M6PR aptamer-FQD$_2$647. **b**, Representative confocal images of M6PR aptamer-FQD$_2$647-treated cells before and after whole-cell (left) or localized (right) photoactivation. The image size was 50 × 50 μm^2. **c**, A representative confocal image of individual CI-M6PR vesicles tracked in live cells. The image size was 25 × 25 μm^2. **d**, Distribution of diffusion coefficients for individual CI-M6PR vesicles (left). The box plot indicates the median (center line) and the interquartile range (box for the 25^{th}–75^{th} percentiles and whiskers for the 10^{th}–90^{th} percentiles). Curve of averaged MSD vs. time lag (right). The solid line represents a linear fit. 123 vesicles were included in the analysis. For the above confocal experiments, a scanning speed of 97.65 μs/pixel and a pixel size of approximately 190 × 190 nm^2 were used. Photoactivation of 1 frame was performed using a 5% 405-nm laser power. Error bars, the standard error of the mean (SEM). Scale bars, 5 μm. All the live-cell results were obtained in live-cell imaging solution.

Fig. 5 Future applications of FQD probes in super-resolution imaging. a, Incorporating FQD and PhADE into DNA-PAINT suppresses background fluorescence from high concentrations of imager strands in hydrogel-embedded and cleared samples. **b**, Replacing the transient DNA probes with stable ones allows PALM imaging in fixed cells.

Figures

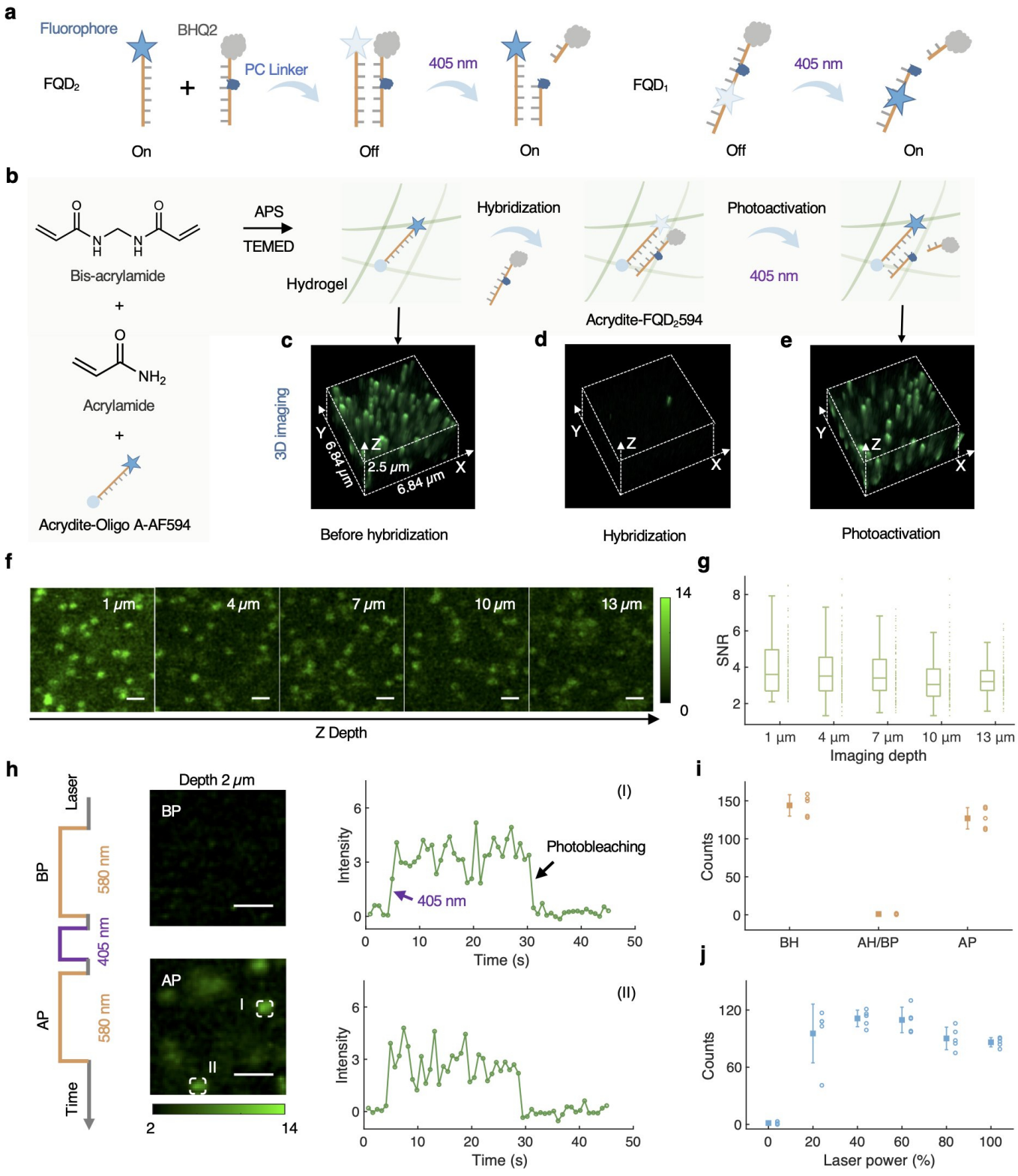


Figure 1

Deep volumetric single-molecule imaging of Acrydite-FQD$_2$594 immobilized within a hydrogel matrix.
a, Structures of FQD$_1$ and FQD$_2$ probes. FQD$_2$ represents the bimolecular construct annealed of two

complementary oligo strands, whereas FQD_1 denotes the unimolecular construct made of a single oligo strand. **b**, Preparation workflow of anchoring Acrydite-$FQD_2$594 in a polyacrylamide hydrogel during the polymerization process. **c-e**, Representative volumetric confocal reconstructions of $FQD_2$594 molecules revealing that Acrydite-Oligo A-AF594 is immobilized in the hydrogel matrix (**c**); subsequent hybridization with the PC Linker and BHQ2-modified Oligo B yields $FQD_2$594 in the non-fluorescent “off” state (**d**); upon photoactivation, the PC Linker undergoes cleavage and BHQ2 hence dissociates, converting $FQD_2$594 to the fluorescent "on" state (**e**). Images were acquired using the Z-Stack mode. The image size was 6.84 × 6.84 × 2.5 mm^3, with a Z-step size of 0.5 mm covering a Z-range of 2.0–4.5 mm (relative to the coverslip surface at 0 mm). Both hydrogel polymerization and oligo hybridization were conducted in 1X PBS buffer (pH 7.4). **f**, Confocal images of $FQD_2$594 at varying Z depths. The image size was 6.84 × 6.84 mm^2. **g**, Statistics of the SNR of $FQD_2$594 molecules across different imaging depths. 3 random imaging regions (6.84 × 6.84 mm^2) with 75–98 molecules were analyzed per Z depth. **h**, Representative single-molecule images of $FQD_2$594 before (BP) and after (AP) photoactivation. The imaging depth was 2 mm, and the image size was 3.42 × 3.42 mm^2. **i**, Single-molecule intensity trajectories corresponding to the specific spots (I, II) annotated in the images in **h**. **j**, Quantification of the average spot counts per imaging area before hybridization (BH), after hybridization/before photoactivation (AH/BP), and after photoactivation (AP). 5 random imaging regions (Z depth at 2 mm, 13.76 × 13.76 mm^2) were analyzed per condition. **k**, Quantification of the average spot counts of photoactivated $FQD_2$594 per imaging area at different 405-nm laser powers. 5 random imaging regions (Z depth at 2 mm, 13.76 × 13.76 mm^2) were analyzed per condition. For the above confocal experiments, a scanning speed of 97.65 ms/pixel and a pixel size of 53.84 × 53.84 nm^2 were used. Photoactivation of 1 frame (equivalent to a single-molecule activation time of 4.78 ms per frame) was performed using a 20% 405-nm laser power unless otherwise specified. Error bars, the standard deviation (SD). Scale bars, 1 mm. All the single-molecule images were obtained in Buffer B, and 1X Gloxy was added before imaging.

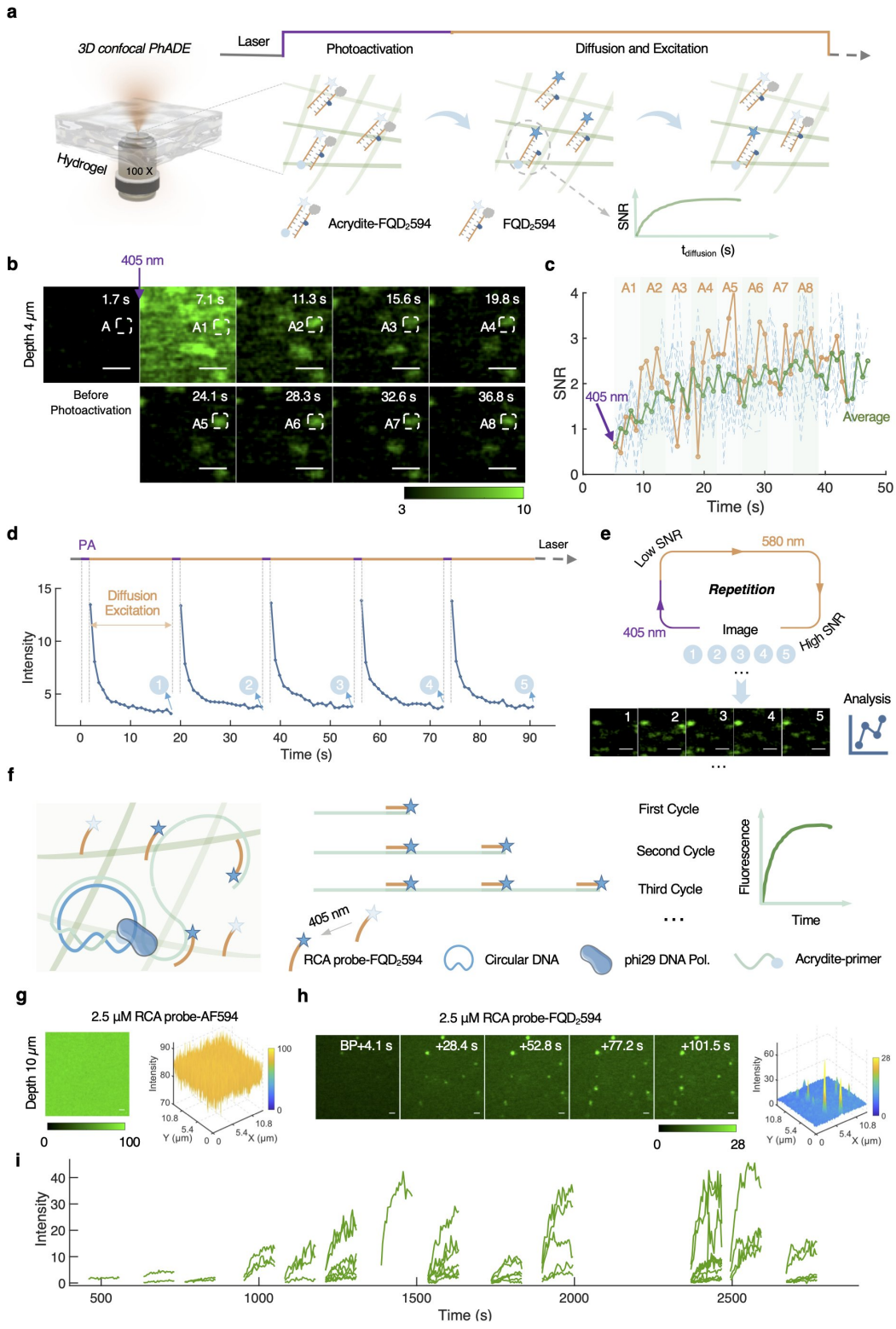


Figure 2

Deep volumetric confocal PhADE imaging. a, Principle of deep volumetric confocal PhADE imaging. Acrydite-FQD$_2$594 is immobilized, while diffusing FQD$_2$594 is infused into the hydrogel. Upon photoactivation (405 nm), both the immobilized Acrydite-FQD$_2$594 and the diffusing FQD$_2$594 near the focal spot are converted to the “on” state. During excitation (580 nm), the non-immobilized FQD$_2$594 diffuses out of the imaging volume, leading to a time-dependent increase in the SNR of the immobilized

Acrydite-$FQD_2$594. **b**, Deep volumetric confocal PhADE imaging of Acrydite-$FQD_2$594 immobilized in a hydrogel matrix with 1 mM diffusing $FQD_2$594 (one PhADE cycle). The imaging depth was 4 mm, and the image size was 3.42 × 3.42 mm^2. Each image represents an average of five raw frames, corresponding to the time periods (A1–A8) annotated in **c**. **c**, Time-dependent SNR for the immobilized Acrydite-$FQD_2$594 in a single PhADE cycle. "Point A" denotes the specific spot marked in **b**; "Average" represents the mean SNR over all identified spots (n = 9). For the confocal experiments in **a-c**, a scanning speed of 97.65 ms/pixel and a pixel size of 53.84 × 53.84 nm^2 were used. Photoactivation of 2 frames (equivalent to a single-molecule activation time of 4.78 ms per frame) was performed using a 20% 405-nm laser power in **a-c**. **d**, Intensity decay curves of background fluorescence in continuous PhADE cycles at 1 mM $FQD_2$594. The double-exponential decay time constants were 0.6 s and 4.0 s, respectively. For the confocal experiments in **d**, a scanning speed of 97.65 ms/pixel and a pixel size of 53.84 × 53.84 nm^2 were used. Photoactivation of 2 frames (equivalent to a single-molecule activation time of 4.78 ms per frame) was performed using a 20% 405-nm laser power in **d**. The duration of diffusion and excitation was 20 frames. **e**, Workflow and representative images of deep volumetric confocal PhADE imaging (continuous PhADE cycles). **f**, Workflow of observing individual RCA reactions in the hydrogel with deep volumetric confocal PhADE imaging. The RCA initiation complex, consisting of the Acrydite-labeled RCA primer and the circular RCA template, is copolymerized into the hydrogel network, followed by the infusion of RCA probe-$FQD_2$594. The RCA reaction is initiated by the addition of phi29 DNA Polymerase and dNTPs. As the reaction proceeds, each amplification cycle generates a binding site for RCA probe-$FQD_2$594, resulting in a progressive increase in fluorescence intensity. **g**, Deep volumetric confocal imaging of individual RCA reactions (without PhADE) at 2.5 mM RCA probe-AF594. The imaging depth was 10 mm, and the image size was 13.76 × 13.76 mm^2. Each image represents an average of two raw frames. **h**, Deep volumetric confocal PhADE imaging of individual RCA reactions at 2.5 mM RCA probe-$FQD_2$594 (continuous PhADE cycles). The imaging depth was 10 mm, and the image size was 13.76 × 13.76 mm^2. Each image represents an average of two raw frames. **i**, Fluorescence intensity trajectories representing the growth curves of individual RCA reactions. The addition of phi29 DNA Polymerase and dNTPs was at t = 0 s. 13 consecutive movies were obtained from different regions, with each movie consisting of 25 PhADE cycles. For the confocal experiments in **f-i**, a scanning speed of 9.75 ms/pixel and a pixel size of 53.84 × 53.84 nm^2 were used. Photoactivation of 1 frame (equivalent to a single-molecule activation time of 4.78 ms per frame) was performed using a 20% 405-nm laser power in **f-i**. The duration of diffusion and excitation was 2 frames (approximately 2.6 s). Scale bars, 1 mm. All the single-molecule images in **a-e** were obtained in Buffer B, and 1X Gloxy was added before imaging. All the single-molecule results in **f-i** were obtained in Buffer D, and 1X Gloxy was added before imaging.

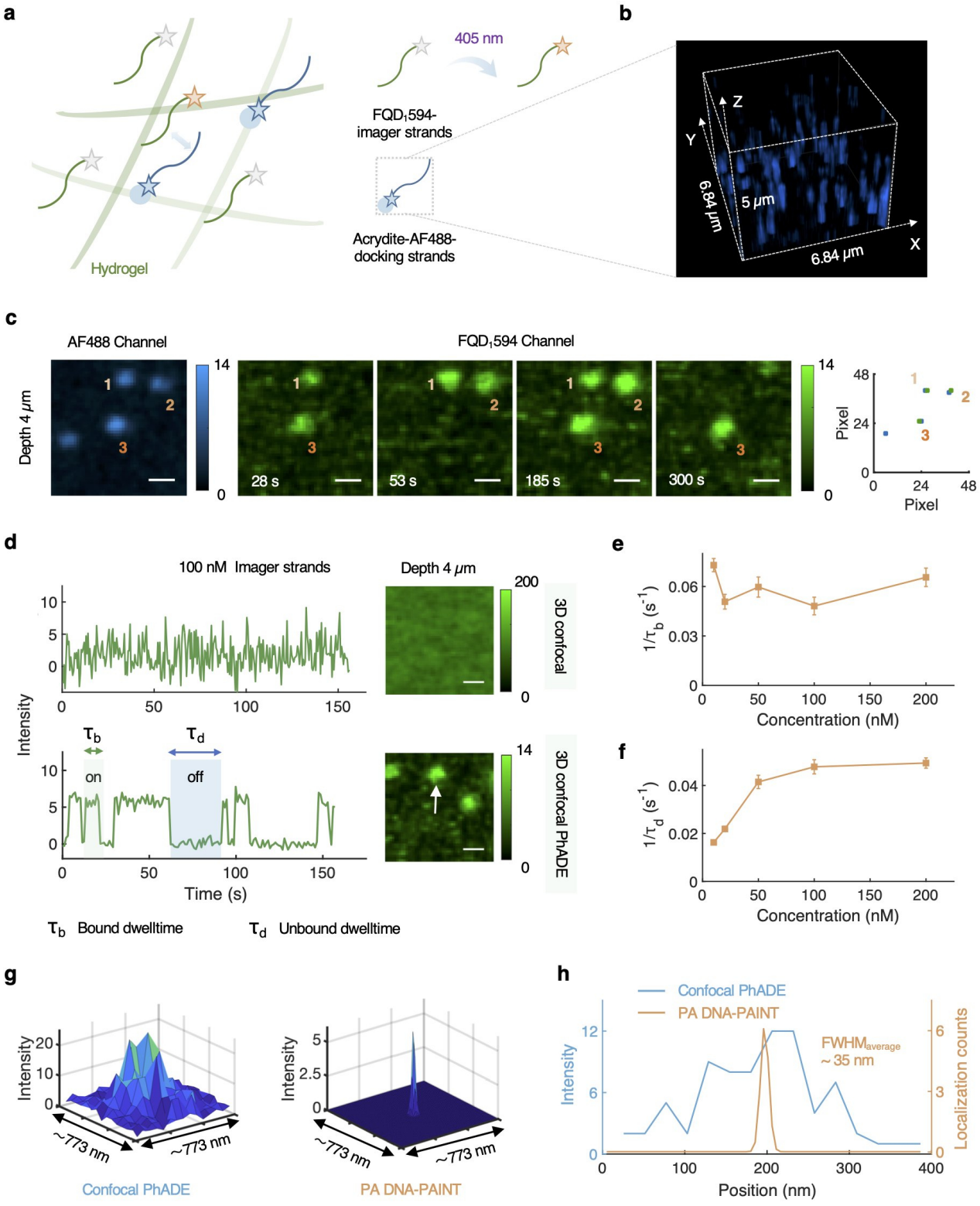


Figure 3

Deep volumetric confocal PhADE imaging of single DNA hybridization events. a, Workflow of observing single DNA hybridization events in the hydrogel with deep volumetric confocal PhADE imaging. The FQD_1594-labeled imager strands interact with the Acrydite-AF488-labeled docking strands in the hydrogel. **b**, A representative volumetric confocal reconstruction revealing that the Acrydite-AF488-docking strands are immobilized in the hydrogel matrix. Images were acquired using the Z-Stack mode.

The image size was 6.84 × 6.84 × 5 mm^3, with a Z-step size of 1 mm covering a Z-range of 2.0–7.0 mm (relative to the coverslip surface at 0 mm). **c**, Co-localization analysis between the AF488 channel (left) and the $FQD_1$594 channel (middle), and the co-localized pixel positions (right). The imaging depth was 4 mm, and the image size was 2.42 × 2.42 mm^2. **d**, Representative intensity trajectories with the unbound or dissociated state (t_d) and the bound state (t_b). Comparison between the confocal mode (top) and the confocal PhADE mode (bottom). **e**, Rate of dissociation ($k_{off} = 1/t_b$) as a function of the $FQD_1$594-imager strand concentration. **f**, Rate of binding ($k_{on} = 1/t_d$) as a function of the $FQD_1$594-imager strand concentration. The mean dwelltimes were derived from 3 random groups with 92–259 and 70–194 events in **e,f**, respectively. For the above confocal experiments, a scanning speed of 102.38 ms/pixel and a pixel size of 51.53 × 51.53 nm^2 were used. Photoactivation of 1 frame (equivalent to a single-molecule activation time of 5.01 ms per frame) was performed using a 20% 405-nm laser power. The duration of diffusion and excitation was 1 frame (approximately 0.52 s). Error bars, the standard deviation (SD). Scale bars, 0.5 mm. All the single-molecule results were obtained in Buffer C, and 1X Gloxy was added before imaging.

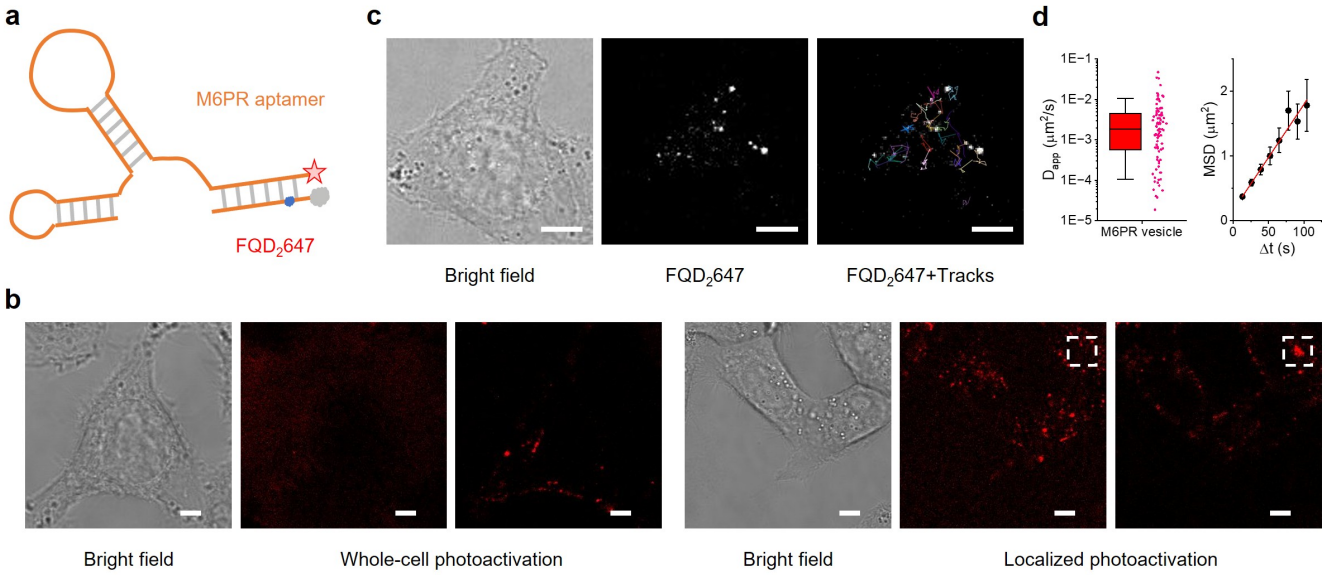


Figure 4

Live-cell tracking of individual CI-M6PR vesicles. a, Structure of M6PR aptamer-$FQD_2$647. **b**, Representative confocal images of M6PR aptamer-$FQD_2$647-treated cells before and after whole-cell (left) or localized (right) photoactivation. The image size was 50 × 50 mm^2. **c**, A representative confocal image of individual CI-M6PR vesicles tracked in live cells. The image size was 25 × 25 mm^2. d, Distribution of diffusion coefficients for individual CI-M6PR vesicles (left). The box plot indicates the median (center line) and the interquartile range (box for the 25th–75th percentiles and whiskers for the 10th–90th percentiles). Curve of averaged MSD vs. time lag (right). The solid line represents a linear fit. 123 vesicles were included in the analysis. For the above confocal experiments, a scanning speed of 97.65 ms/pixel and a pixel size of approximately 190 × 190 nm^2 were used. Photoactivation of 1 frame

was performed using a 5% 405-nm laser power. Error bars, the standard error of the mean (SEM). Scale bars, 5 mm. All the live-cell results were obtained in live-cell imaging solution.

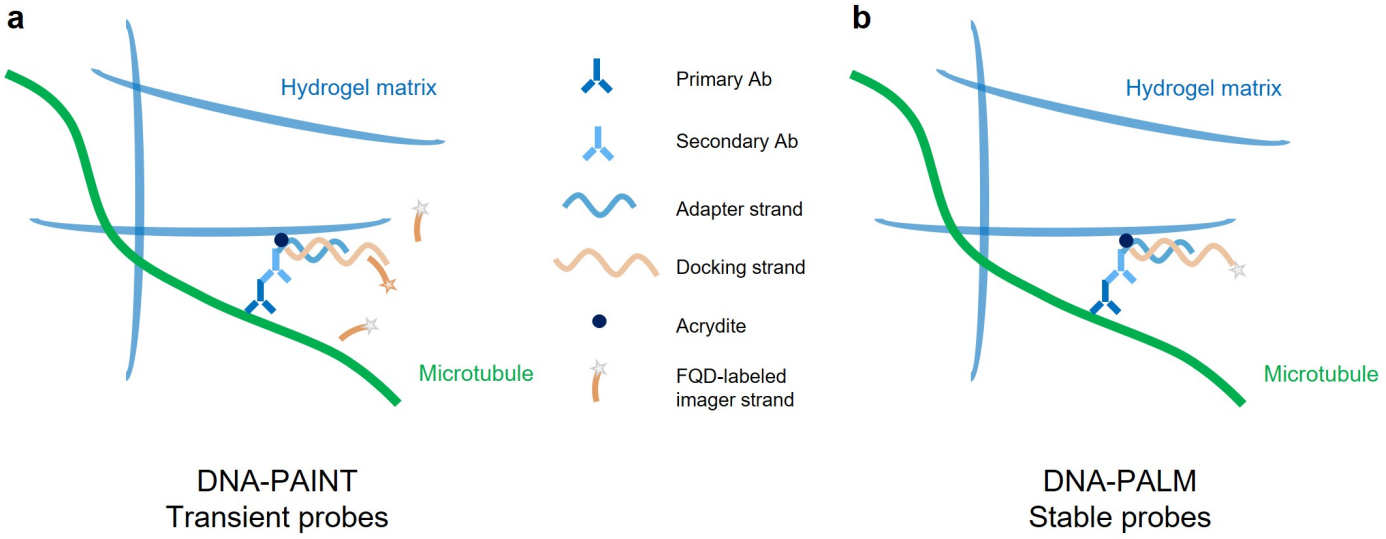


Figure 5

Future applications of FQD probes in super-resolution imaging. a, Incorporating FQD and PhADE into DNA-PAINT suppresses background fluorescence from high concentrations of imager strands in hydrogel-embedded and cleared samples. **b**, Replacing the transient DNA probes with stable ones allows PALM imaging in fixed cells.

Supplementary Files

This is a list of supplementary files associated with this preprint. Click to download.

- PAfluorescentprobesSI33.docx
- figures1figure1.jpg
- figures2figure1.jpg
- figures3figure2.jpg
- figures4figure2.jpg
- figures5figure2.jpg
- figures6figure2.jpg
- figures7figure3.jpg